Check for updates

ADVANCED MATERIALS
www.advmat.de

Flash-Thermal Shock Synthesis of High-Entropy Alloys Toward High-Performance Water Splitting

Jun-Hwe Cha, Su-Ho Cho, Dong-Ha Kim, Dogyeong Jeon, Seohak Park, Ji-Won Jung, Il-Doo Kim,* and Sung-Yool Choi**

High-entropy alloys (HEAs) provide unprecedented physicochemical properties over unary nanoparticles (NPs). According to the conventional alloying guideline (Hume–Rothery rule), however, only size-and-structure similar elements can be mixed, limiting the possible combinations of alloying elements. Recently, it has been reported that based on carbon thermal shocks (CTS) in a vacuum atmosphere at high temperature, ultrafast heating/cooling rates and high-entropy environment play a critical role in the synthesis of HEAs, ruling out the possibility of phase separation. Since the CTS requires conducting supports, the Joule-heating efficiencies rely on the carbon qualities, featuring difficulties in uniform heating along the large area. This work proposes a photo-thermal approach as an alternative and innovative synthetic method that is compatible with ambient air, large-area, remote process, and free of materials selection. Single flash irradiation on carbon nanofibers induced momentary high-temperature annealing (>1800 °C within 20 ms duration, and ramping/cooling rates >10^4 K s^{-1}) to successfully decorate HEA NPs up to nine elements with excellent compatibility for large-scale synthesis (6.0 × 6.0 cm^2 of carbon nanofiber paper). To demonstrate their feasibility toward applications, senary HEA NPs (PtIrFeNiCoCe) are designed and screened, showing high activity ($\eta_{overall}$ = 777 mV) and excellent stability (>5000 cycles) at the water splitting, including hydrogen evolution reactions and oxygen evolution reactions.

1. Introduction

High-entropy alloys (HEAs) consisting of at least five elements offer unprecedented physicochemical properties, which could exceed single-element (or unary) nanoparticles (NPs), especially for metal-based catalysts.[1] In addition, alloying multiple metallic elements allows for a broad selection of elements, including precious and nonprecious metals, leading to high thermal/chemical stability and striking catalytic activity for various applications.[2] However, the Hume-Rothery rule has conventionally been introduced as the essential conditions for bulk alloy formation in terms of atomic size difference, atomic structure, valences, and electronegativity. According to this alloying guideline, only similar elements can be mixed, thereby limiting the range of the possible alloy element combinations for the synthesis of HEA particles, especially with nanosized particles (<10 nm).

To overcome the aforementioned issues, providing an extremely high-temperature and high-entropy environment can be a breakthrough strategy for the synthesis of HEA NPs with compositions that were previously considered to be non-miscible based on traditional alloying theories. Especially, introducing high temperatures, ultrafast heating/cooling rates, and mixing various compositional elements might play a critical role in the successful synthesis of HEAs based on high entropy of mixing within a short time, thereby ruling out the possibility of phase separation. However, achieving atomic scale mixing for HEA NPs using the traditional furnace annealing approaches is challenging because of their sluggish heating/cooling rates. Therefore, the development of an

J.-H. Cha, S. Park, S.-Y. Choi
School of Electrical Engineering
Korea Advanced Institute of Science and Technology
291 Daehak-ro, Yusenong-gu, Daejeon 305–701, Republic of Korea
E-mail: sungyool.choi@kaist.ac.kr

S.-H. Cho, D.-H. Kim[+], D. Jeon, I.-D. Kim
Department of Materials Science and Engineering
Korea Advanced Institute of Science and Technology (KAIST)
291 Daehak-ro, Yuseong-gu, Daejeon 34141, Republic of Korea
E-mail: idkim@kaist.ac.kr

S.-H. Cho, D.-H. Kim[+], D. Jeon, I.-D. Kim
Advanced Nanosensor Research Center
KI Nanocentury
KAIST
291, Daehak-ro, Yuseong-gu, Daejeon 34141, Republic of Korea

J.-W. Jung
School of Materials Science and Engineering
University of Ulsan (UOU)
12, Technosaneop-ro 55 beon-gil, Nam-gu, Ulsan 44776, Republic of Korea
E-mail: jwjung4@ulsan.ac.kr

The ORCID identification number(s) for the author(s) of this article can be found under https://doi.org/10.1002/adma.202305222

[+]Present address: Department of Chemistry, Massachusetts Institute of Technology, 77 Massachusetts Avenue, Cambridge, MA 02139, USA

DOI: 10.1002/adma.202305222

 © 2023 Wiley-VCH GmbH

alternative momentary annealing technique is highly required.

Yao et al. have recently proposed a new approach for the formation of HEA NPs by the introduction of an innovative carbon thermal shocks (CTS)-based method which relies on Joule-heating processes to enable momentary heating (temperature > 2000 K and ramping/cooling rates >10^5 K s^{-1}). The CTS method significantly expands the range of available transition metal alloys, allowing for the synthesis of previously unapproachable alloy structures.[3] In addition, the CTS method has been successfully exploited for various applications such as synthesis of single atoms and HEA NPs in the form of metals, oxides, and sulfides showing great promise for rapid and facile synthesis.[4] In spite of the novel strengths of the CTS approach, its implementation is limited to the use of conducting materials and by formation of electrode contacts onto carbon-based conducting supports to enable sufficient current flow for Joule heating in vacuum systems. In addition, the Joule-heating efficiencies greatly rely on the carbon qualities, resulting in difficulties in uniform heating across a large area. Beyond the CTS method, an alternative and innovative synthetic approach compatible with ambient air, large-area, remote process, and free of materials selection is highly required.

Photo-thermal effects are typically known as light-material interaction leading to energy exchange between photons from incident light and electrons in materials. As a consequence, photo-excited electrons could generate phonons and form thermal energies in any light-exposed parts of materials, enabling mass-productive synthesis covering the area of light beam sources.[5] In general, the light-induced heating approach is typically employed for metals or black-colored materials (e.g., carbon, black oxides, etc.) with small band gaps, which usually feature high photothermal efficiencies. However, recent reports have demonstrated that even white-colored metal oxides with high band gaps (>3 eV) can exhibit a remarkable photothermal effect (>1800 °C in 20 ms duration) through the elaborate tuning of defect density.[3] Consequently, non-contact interaction between light and support materials holds great promise as a breakthrough strategy for the mass- and time-productive approach, showing great potential for facile, versatile, and ambient synthesis of catalysts.

In this work, we demonstrate the ambient-air, large-area, and remote synthesis for HEA NPs through the photothermal effects induced by light irradiation on carbon-based supports exemplified by carbon nanofibers (CNFs). Single flash irradiation on CNFs induced momentary high-temperature annealing (>1800 °C within 20 ms duration, and ramping/cooling rates >10^4 K s^{-1}) to successfully decorate HEA NPs up to nine elements with excellent compatibility for large-scale synthesis (6.0 × 6.0 cm^2 of CNF paper). Interestingly, 2D materials, e.g., MXenes and graphene oxides, also demonstrate similar support capabilities to the CNFs, highlighting the broad selection of support materials available for this method. To demonstrate the practical applications of these HEA NPs, we designed and screened senary HEA NPs (PtIrFeNiCoCe) for high activity ($\eta_{overall}$ = 777 mV) and excellent stability (>5000 cycles) in the water splitting, including hydrogen evolution reaction (HER) and oxygen evolution reactions (OER). Our results are highly encouraging, as they clearly demonstrate that the use of a remote approach between light and support materials is a promising and productive synthesis method, which offers numerous benefits. First, it is highly efficient in terms of both mass and time productivity. Second, it is compatible with ambient air, allowing for a more convenient and cost-effective approach for the uniform synthesis of multi-metal catalysts. Additionally, it can cover a large-area process, making it suitable for industrial-scale applications. Finally, it is free from materials selection constraints, which allows for a wider range of materials to be utilized in the synthesis process.

2. Results and Discussion

Figure 1a illustrates the non-contact, large area, and ambient-air synthetic method of high-entropy-alloy nanoparticles (HEA NPs) through the millisecond-scale (<20 ms) flash-thermal shock (FTS) lamping via a xenon lamp. First, carbon nanofibers (CNF) membranes, which are synthesized by electrospinning followed by high-temperature pyrolysis, were soaked and coated with multi-component metal precursors. Note that in spite of a broad range of support materials, the CNFs membranes were introduced for an actual demonstration of mass production. The resultant CNF membranes were put on the stage and exposed to the flashlight with an energy density of 4.9 J cm^{-2} for 20 ms. During the process, the FTS lamping (4.9 J cm^{-2}) led to photon-electron couplings and energy exchange between the incoming photons and phonons in the carbon lattice via non-radioactive recombination processes. As a result of the single flash irradiation, the surface temperature of CNF membranes could increase up to 1800 °C within 5 ms, providing sufficient energies for precursor decomposition and fission/fusion of transient liquid metal particles on the surface of the CNFs strands.[6] The following rapid cooling process (>6.7 × 10^4 K s^{-1}) enabled the synthesis of HEA NPs through minimization of phase separation. It is noteworthy that the uniform catalytic NPs could be formed in entire CNF membranes when the sample is treated with FTS on both sides of the CNF membranes (Figure S1, Supporting Information). In addition, the quality of carbon in CNF membranes can affect the sizes and distribution of HEA NPs at the same FTS lamping due to variations in the distribution and density of defective points on the surface of CNF membranes (Figure S2, Supporting Information). Herein, it was confirmed that the HEA NPs can be composed of up to 9 cations from Pt, Ir, Fe, Ni, Co, La, Ce, In, and Sr precursors, indicating the potential of the FTS lamping for various applications requiring HEA NPs with diverse compositions. The suggested FTS-induced HEA synthetic method is applicable not only to CNFs but also to diverse 2D materials such as MXenes and graphene oxides, highlighting its potential for various applications. To analyze the temperature–time profile of the sample surface, we implemented a momentary temperature measurement set-up that utilized dual infrared (IR) sensors (1500-sensor and 3000-sensor) as shown in Figure 1b. The 1500-sensor and 3000-sensor can measure temperatures in the range of 200–1500 °C and 1500–3000 °C, respectively, according to the equipment specification. It is a well-known fact that heating carbon materials enables the emission of IR elements with an emissivity of 0.79. Accordingly, the 1500-sensor and 3000-sensor with detectable wavelengths of 2.3 and 1.5 μm, respectively, can detect the IR information and convert the analog signals into current forms. IR noise effects from the lamp were confirmed to be negligible, although Xe lamp could generate broad-spectrum light even with an infrared spectrum above the wavelength of 0.8 μm

© 2023 Wiley-VCH GmbH

15214095, 2023, 46, Downloaded from https://onlinelibrary.wiley.com/doi/10.1002/adma.202305222 by Shanxi University, Wiley Online Library on [06/11/2024]. See the Terms and Conditions (https://onlinelibrary.wiley.com/terms-and-conditions) on Wiley Online Library for rules of use; OA articles are governed by the applicable Creative Commons License

15214095, 2023, 46, Downloaded from https://onlinelibrary.wiley.com/doi/10.1002/adma.202305222 by Shanxi University, Wiley Online Library on [06/11/2024]. See the Terms and Conditions (https://onlinelibrary.wiley.com/terms-and-conditions) on Wiley Online Library for rules of use; OA articles are governed by the applicable Creative Commons License

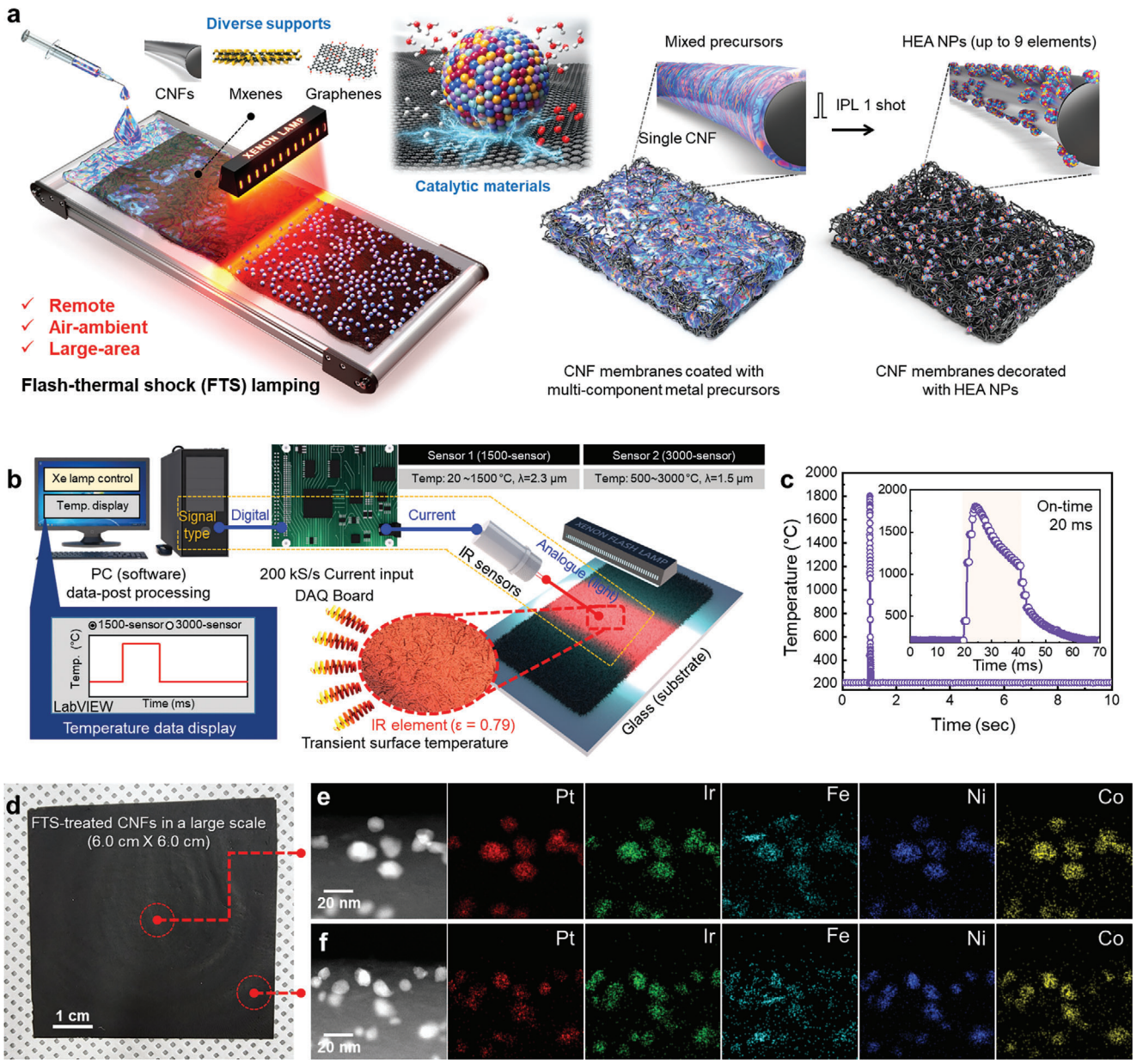

Figure 1. a) Schematic illustration of the noncontact, mass-productive, and ambient-air synthetic method of HEA-NPs through the millisecond-scale (<20 ms) light pulse irradiations generated by a xenon lamp. b) Schematic illustration of the momentary temperature measurement set-up using dual IR sensors of 1500-sensor and 3000-sensor. c) Temperature–time curves of the CNF membranes coated with multi-component metal precursors at the 20 ms flash lamping with light energy densities of 4.9 J cm^{-2}. d) Photoimage of the FTS-treated CNFs on a large scale at the 20 ms flash lamping with light energy densities of 4.9 J cm^{-2} with precursors of five dissimilar elements (Pt, Ir, Fe, Ni, and Co). e,f) EDS elemental mapping images of center (e) and edge (f) parts of the FTS-treated CNFs.

(Figure S3, Supporting Information). As the next step, the information on the current input transformed from the IR sensor was collected into a data acquisition (DAQ) board with a sample rate of 200 kS s^{-1}. This enabled the acquisition of the IR information emitted from the heating samples at a time resolution of 5 μs, which was sufficient for continuous data recording (Figure S4, Supporting Information). Eventually, digital information on the materials' temperature was obtained as the final data output. It should be noted that the emissivity of materials was set as unity for the measurement, meaning that emissivity correction should be subsequently performed. For true temperature of samples, it is normally known to be related to spectral emissivity and a black body temperature shown below as Equation (1).[7]

$$\frac{1}{T} = \frac{\lambda}{C_2} \ln\left(\varepsilon_\lambda \left(e^{C_2/\lambda T_\lambda} - 1\right) + 1\right) \tag{1}$$

where T is the true temperature, λ indicates the detectable wavelength of the IR sensors, C_2 represents the second radiant constant 14 388 μm K^{-1}, and T_λ is temperature of a black body

 © 2023 Wiley-VCH GmbH

having emissivity of 1.00, and $\epsilon\lambda$ represents the spectral emissivity defined as the ratio of the real emissivity from a measuring sample to unity from the black body. Since sample and measurement conditions meet Wien's approximation ($C_2/\lambda T_\lambda \gg 1$) resulting from high emissivity of 0.79 (>0.5), short detector wavelength of 2.3 µm (1500-sensor) and 1.5 µm (3000-sensor), and low temperature (<1500 K), Equation (1) can be simplified into Equation (2) below.

$$\frac{1}{T} = \frac{1}{T_\lambda} + \frac{\lambda}{C_2}\ln\varepsilon_\lambda \tag{2}$$

Consequently, temperature data detected with emissivity of unity can be corrected by Equation (3), given that the spectral emissivity is equal to real emissivity of samples over emissivity of unity ($\epsilon_{\text{corrected}}/\epsilon_{\text{measured}}$).

$$\frac{1}{\mathrm{T}_{\text{corrected}}} = \frac{1}{\mathrm{T}_{\text{measured}}} + \frac{\lambda_{\text{detect}}\ln\left(\varepsilon_{\text{corrected}}/\varepsilon_{\text{measured}}\right)}{C_2} \tag{3}$$

where $T_{\text{corrected}}$ means corrected temperature with the materials emissivity ($\epsilon_{\text{corrected}}$), T_{measured} indicates measured temperature with the IR sensor at the emissivity of 1.00 ($\epsilon_{\text{measured}}$), and λ_{detect} represents a detectable wavelength of the IR sensors. Figure 1c shows the transient-temperature curve of the CNF membranes coated with multi-component metal precursors at the 20 ms flash lamping with light energy density of 4.9 J cm^{-2}. The corrected and modified analog data measured by the dual IR sensors displayed that the surface temperature of the CNF membranes soared above 1800 °C within 5 ms (For more details, see Figure S5, Supporting Information). Subsequently, it started to gradually decrease for the rest of the on-time (15 ms) in the range above 1000 °C. Finally, sharp temperature drop was observed for 30 ms down to the minimum measurable temperature (baseline) of 200 °C, exhibiting ultrafast ramping/cooling rates higher than 10^4 K s^{-1}. The millisecond-scale heating of CNF strands results in the formation of HEA NPs on the surface in an air-ambient and the noncontact manner. The detailed mechanism behind this process will be discussed in the following section. To demonstrate the potential for large-area and mass-production applications using the FTS lamping, a CNF membrane with an area of 6.0 cm × 6.0 cm was prepared and exposed to a single flash light with an energy density of 4.9 J cm^{-2} from the large-area (10.0 cm × 15.0 cm) lamp with a beam reflector. This configuration enabled a uniform FTS process over the entire area. Given that lengths of flash lamps can be expanded up to meters, the FTS process could give great promise of high-throughput mass-production toward the synthesis of HEA NPs.[5] Figure 1d shows a photo image of the FTS-treated CNFs on a large scale with precursors of five dissimilar elements (Pt, Ir, Fe, Ni, and Co). We verified the uniformity of the FTS process even on a large scale by confirming the homogeneous formation of quinary HEA NPs (PtIrFeNiCo) both on the center and edge of the FTS-treated CNFs through energy-dispersive X-ray spectroscopy (EDS) analysis (Figure 1e,f).

Next, we demonstrated the versatility and effectiveness of the suggested FTS method in preparing various compositions of HEA NPs (**Figure 2**). First, we investigated the influence of the concentration of metal ion precursors on particle size and density, which are coated on the CNF membranes prior to the FTS process. Three different concentrations of Pt precursors, i.e., 0.03, 0.05, and 0.10 M, respectively, were coated on the CNF membranes on which FTS was conducted to synthesize CNF membranes decorated with Pt NPs. As a result, high precursor concentration (0.10 M) resulted in excessive growth of Pt NPs (≈200 nm) and a high loading amount of 16.7 wt%, while adequate concentrations (0.03 and 0.05 M) led to the formation of uniformly distributed sub-10 nm Pt NPs with loading amounts of 6.7 and 11.1 wt, respectively (Figure S6 and Table S1, Supporting Information). Thus, we concluded that 0.05 M of metal precursors was the optimal concentration, and all the additional experiments were conducted using the same precursor concentrations. Following the optimal conditions, we demonstrated that ultra-high density and uniformly distributed catalytic Pt NPs can be stabilized on CNF substrates during the FTS process (Figure 2a,b). We further confirmed the formation of binary metal NPs (PtCu, PtRu, and PtPd, Figure 2c–e). A nearly 1:1 atomic percentage ratio between Pt:Cu, Pt:Ru, and Pt:Pd in the binary NPs was obtained from EDS mapping analysis (Figure S7, Supporting Information). The composition of catalytic NPs can be extended to ternary (PtCuRu and FeNiCo, Figure 2f,g), quinary (PtIrFeNiCo, Figure 2h,i), octonary (PtIrFeCoNiPdCuRu, Figure S8, Supporting Information), and even novenary (PtIrFeNiCoLaCeInSr, Figure 2j) based on rapid heating/cooling processes and a considerable increase in the entropic contribution for HEA NPs formation through introduction of various metal elements.[8] In this regard, the successful synthesis of HEA NPs with numerous compositions, such as PtIrFeNiCoLaCeInSr, would show huge potential for broadening the application toward various catalytic effects. We provided additional evidence of homogeneous element mixing in HEA NPs by utilizing CNF membranes decorated with PtIrFeNiCo NPs (Figure S9, Supporting Information). The results revealed a uniform distribution of each element, with the atomic percentage distribution of Pt (19.61% ± 4.77%), Ir (21.24% ± 5.00%), Fe (20.81% ± 5.00%), Ni (13.02% ± 5.17%), and Co (25.40% ± 1.32%) (Table S2, Supporting Information). To further validate the chemical states and crystal structures of the HEA NPs, we conducted X-ray photoelectron spectroscopy (XPS) and X-ray diffraction (XRD) analyses using CNF@PtIrFeCoNiPdCuRu samples. The XPS analysis of CNF@PtIrFeCoNiPdCuRu showed a combination of metallic and oxidized states for each element (see Figure S10, Supporting Information). However, the XRD analysis demonstrated the bulk crystalline properties of PtIrFeCoNiPdCuRu, revealing a highly crystalline face-centered-cubic single-phase alloy structure (see Figure S11, Supporting Information).

The strength of the FTS method lies in its ability to use any materials as heating substrates as long as they feature high photothermal efficiencies. To demonstrate this, we additionally prepared 2D materials including graphene oxides and MXenes as heating substrates for the synthesis of HEA NPs through photothermal heat, which is induced by light irradiation. After coating Pt, Ir, Fe, Ni, and Co precursors on graphene oxide and MXenes, respectively, subsequent FTS lamping led to the formation of uniform and high-density PtIrFeNiCo HEA NPs on reduced graphene oxide and MXenes (Figure 2k–n). It is well-known that graphene oxide is readily transformed into reduced graphene oxide upon light irradiation.[9] Such broadening of not only

© 2023 Wiley-VCH GmbH

15214095, 2023, 46, Downloaded from https://onlinelibrary.wiley.com/doi/10.1002/adma.202305222 by Shanxi University, Wiley Online Library on [06/11/2024]. See the Terms and Conditions (https://onlinelibrary.wiley.com/terms-and-conditions) on Wiley Online Library for rules of use; OA articles are governed by the applicable Creative Commons License

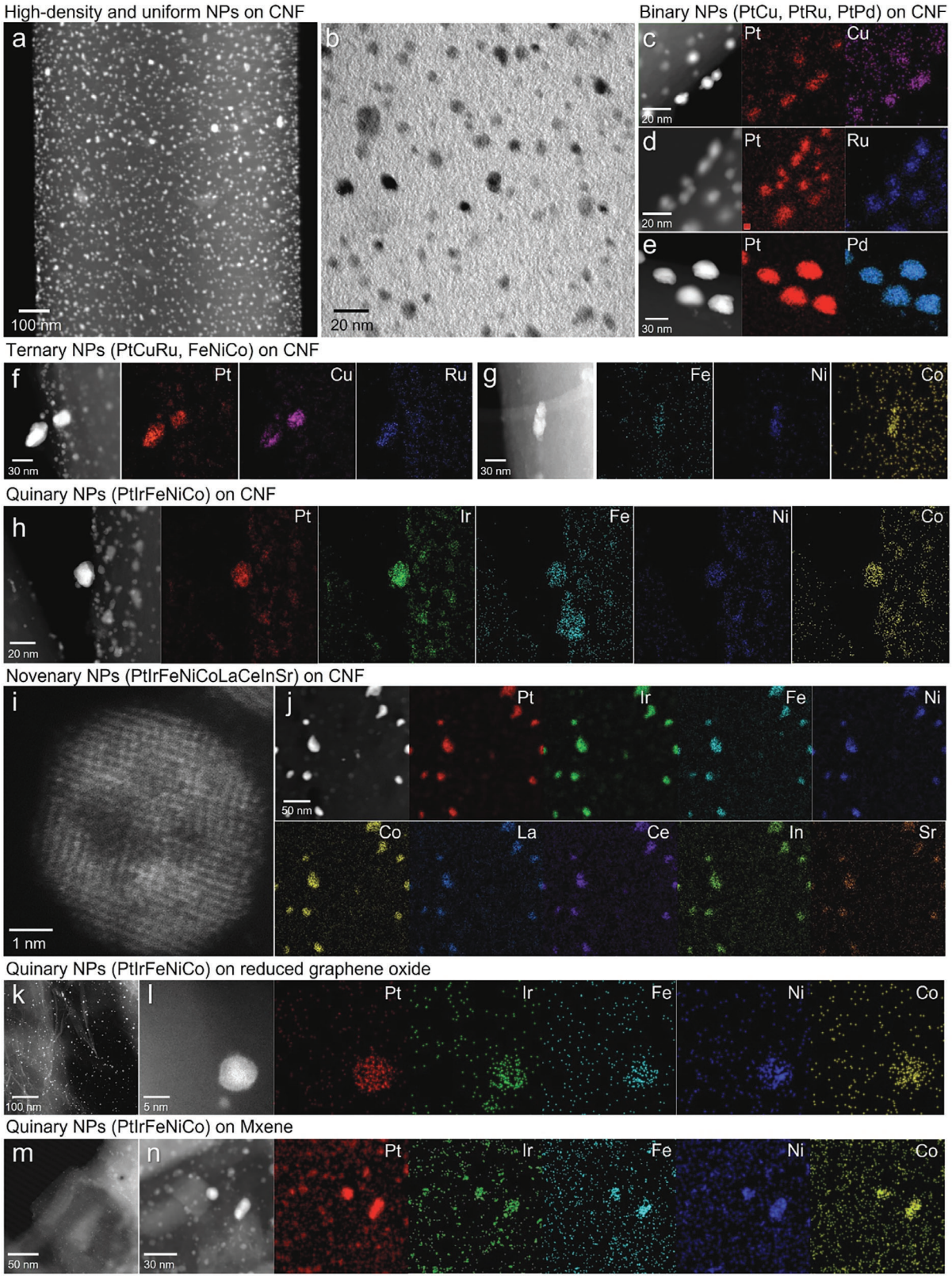

Figure 2. a) STEM and b) TEM images of CNF decorated with Pt NPs. STEM and EDS mapping images of CNF decorated with binary NPs; c) PtCu, d) PtRu, and e) PtPd. STEM and EDS mapping images of CNF decorated with ternary NPs; f) PtCuRu, and g) FeNiCo. h) STEM and EDS mapping images of CNF decorated with quinary NPs; PtIrFeNiCo and i) HRTEM image. j) STEM and EDS mapping images of CNF decorated with novenary NPs; PtIrFeNiCoLaCeInSr. k–n) STEM and EDS mapping images of reduced graphene oxide (k–l) and MXenes decorated with quinary NPs; PtIrFeNiCo (mn).

 © 2023 Wiley-VCH GmbH

15214095, 2023, 46, Downloaded from https://onlinelibrary.wiley.com/doi/10.1002/adma.202305222 by Shanxi University, Wiley Online Library on [06/11/2024]. See the Terms and Conditions (https://onlinelibrary.wiley.com/terms-and-conditions) on Wiley Online Library for rules of use; OA articles are governed by the applicable Creative Commons License

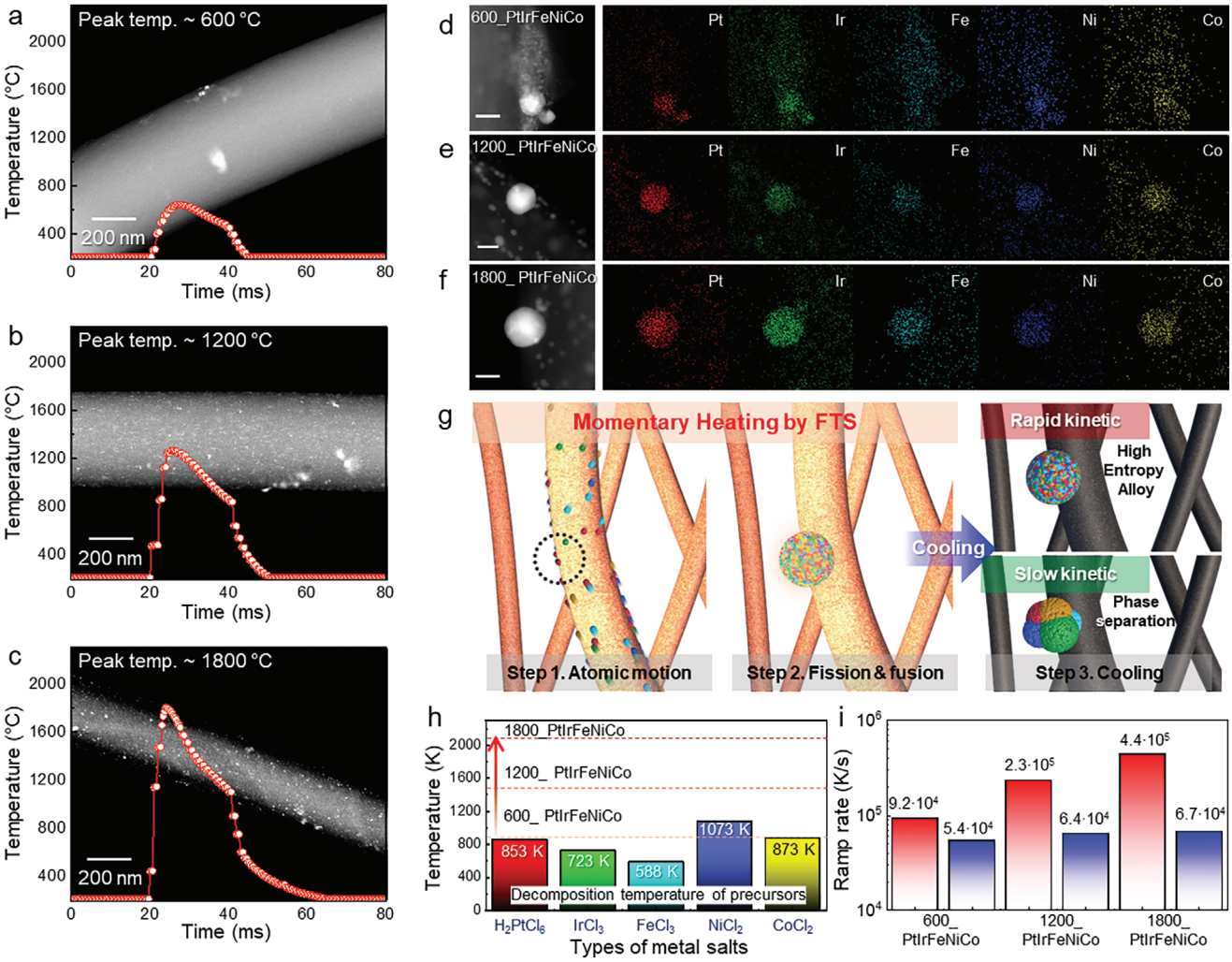

Figure 3. Temperature–time curve of CNF membranes having five dissimilar metal precursors (Pt, Ir, Fe, Ni, Co) FTS-treated with the flashlight with an energy density of a) 1.3, b) 3.2, and c) 4.9 J cm^{-2}. Each condition achieved temperature peaks of 600, 1200, and 1800 °C at the single flashlight, finally making 600_PtIrFeNiCo, 1200_PtIrFeNiCo, and 1800_PtIrFeNiCo, respectively. The background of the transient temperature profile displays TEM images of each CNF strand on the given conditions at a low magnification. STEM images and EDS elemental mapping of d) 600_PtIrFeNiCo, e) 1200_PtIrFeNiCo, and f) 1800_PtIrFeNiCo. Scale bars: 10 nm. g) Schematic images of the formation steps of HEA NPs by FTS lamping. h) Decomposition temperature of each metal precursor. i) Calculated heating and cooling rates at each FTS lamping condition (1.3, 3.2, and 4.9 J cm^{-2}), corresponding to 600_PtIrFeNiCo, 1200_PtIrFeNiCo, and 1800_PtIrFeNiCo samples, respectively.

compositions of HEA NPs but also conducting and active substrates could lead to strong potential feasibility toward the development of high-quality catalytic materials.

Next, sequential synthesis steps for HEA NPs were systematically investigated on various FTS conditions. **Figure 3**a–c displays the temperature–time curve of CNF membranes treated with the FTS method using flashlight with an energy density of 1.3, 3.2, and 4.9 J cm^{-2}, respectively. One can see that each energy leads to a temperature rise up to ≈600, 1200, and 1800 °C, respectively, within 5 ms at the single flashlight. The background of the transient temperature profile displays TEM images of each CNF strand acquired under the specified conditions, captured at low magnification. Under the FTS lamping of 1.3 J cm^{-2}, sparely distributed HEA NPs were observed on the surface of the CNF strand (Figure 3a). On the contrary, high-density dot-like contrasts were clearly verified on the CNF strand obtained at the FTS lamping of 3.2 and 4.9 J cm^{-2}, representing the uniform formation of HEA NPs (Figure 3b,c). For better understanding, EDS elemental mapping analysis of the FTS-treated CNFs was performed (Figure 3d–f). Under the FTS lamping with 1.3 J cm^{-2} (temperature ≈ 600 °C), nonuniform and incomplete mixing of five elements led to the inhomogeneous formation of HEA NPs (i.e., 600_PtIrFeNiCo) (Figure 3d). When irradiated with higher light energies (3.2 and 4.9 J cm^{-2}, temperature ≈1200 and 1800 °C, respectively), sphere-like HEA NPs (1200_PtIrFeNiCo and 1800_PtIrFeNiCo) were synthesized with uniform dispersions of each element. Hu et al. reported that the synthesis of HEA NPs is greatly affected by surface-bound oxygens (O*) on the substrate, catalytic activities of involving elements, and thermodynamic conditions of the momentary heating and rapid kinetics.[6] In more detail, reduction based on carbothermic reactions (C + O* → CO↑) occurs, which is highly

 © 2023 Wiley-VCH GmbH

15214095, 2023, 46, Downloaded from https://onlinelibrary.wiley.com/doi/10.1002/adma.202305222 by Shanxi University, Wiley Online Library on [06/11/2024]. See the Terms and Conditions (https://onlinelibrary.wiley.com/terms-and-conditions) on Wiley Online Library for rules of use; OA articles are governed by the applicable Creative Commons License

determined by O* and the degree of catalytic properties from each metal. Note that carbon can be sufficiently provided by CNFs as the reducing agent. According to the Ellingham diagram, the catalytic effect of the abovementioned carbon metabolism reaction decreases in the given order of Pt, Ir, Fe, Ni, and Co, implying that Co is the least active metal for the reaction. Figure 3g represents the step-by-step schematic images of the formation of HEA NPs via FTS lamping. For step 1, metal precursors are thermally decomposed by the photothermallygenerated heat, followed by the motion of metal catalysts on the surface through O^* and carbothermic reactions. Photothermally generated heat should be higher than the decomposition temperature of metal precursors to initiate the formative mechanisms of HEA NPs (Figure 3h). We introduced chloride-based metal precursor salts, similar to the previous literature.[6] In addition, when the catalytic effects become less for the carbothermal reactions, the atomic motion of metal catalysts occurs less frequently on the surface. As a result, snapshot-like TEM images for HEA NPs formation were obtained when using relatively deficient light density (1.3 J cm^{-2}) as shown in Figure 3d. Interestingly, Pt and Ir, the most active two elements, formed comparably successful and spherical NP morphologies, while Fe, Ni, and Co showed relatively scattered distributions. As long as sufficient thermal energies are generated by FTS lamping, it can drive vigorous particle fission and fusion events, leading to uniform mixtures of diverse elements as shown in step 2 of Figure 3g. The fast cooling rate ($>10^4$ K s^{-1}) is a critical factor in successfully mixing and maintaining the diverse elements in the form of HEA NPs by restricting the formation of thermodynamically stable phases (i.e., phase separations) in the solid-solution NPs, maintaining their lattice structures (step 3 of Figure 3g).[6] Heating and cooling rates of each FTS lamping condition (1.3, 3.2, and 4.9 J cm^{-2}) are higher than 10^4 K s^{-1} (Figure 3i).

The HEA NPs have been advantageous as potential catalysts for hydrogen evolution reactions (HER) and oxygen evolution reactions (OER) of water splitting.[10] The Pt-decorated CNFs synthesized at a higher temperature are more likely to exhibit enhanced electrocatalytic properties with higher electrical conductivity (Figure S12, Supporting Information). Therefore, all HEA NPs were prepared by loading them onto the CNF membranes synthesized at 1500 °C. To evaluate the HER and OER performance, HEA-functionalized CNFs were employed as electrocatalysts in an alkaline (0.1 M KOH) solution utilizing a three-electrode system (**Figure 4**). Prior to the electrocatalyst test, cyclic voltammetry (CV) was performed by cycling between −0.9 V and 0.1 V versus Ag/AgCl to remove any remaining gas and facilitate the electrolyte–electrocatalyst interface (Figure S13, Supporting Information). When used as an electrocatalyst for HER, quinary HEA NPs (PtIrFeNiCo) on CNF (CNF@PtIrFeNiCo) showed an excellent onset potential of 59.8 mV (V vs RHE) and a small overpotential of 139.9 mV at a current density of 10 mA cm^{-2} with a scan rate of 5 mV s^{-1} (Figure 4a). Meanwhile, the CNF@FeNiCo composed of solely ternary transition metal alloy without Pt catalyst exhibits negligible HER performance with huge onset potential and overpotential. The introduction of transition metal elements (Fe, Ni, and Co) into CNF@Pt enables a lower overpotential (211.5 mV) of CNF@PtFeNiCo than CNF@Pt (260.0 mV). When Pt is mixed with such transition metals to form HEA catalysts, the resulting catalysts can exhibit advantages such as increased active sites and binding energy, even at lower Pt content.[10a,11] Interestingly, the addition of Ir to CNF@PtFeNiCo (CNF@PtIrFeNiCo) further reduces the overpotential. Both CNF@Ir and CNF@PtIrFeNoCoCe have similar onset potentials, which are inferior to CNF@PtIrFeNiCo.

The Tafel plots corresponding to the HER performance are displayed in Figure 4b. The Tafel slope of the CNF@PtIrFeNiCoCe is the smallest (91.1 mV dec^{-1}) among the control groups. It is noticeable that the CNF@PtIrFeNiCoCe with senary alloying elements exhibits a significantly faster HER catalytic kinetics with excellent Tafel slope (91.1 mV dec^{-1}) compared with those of the CNF@Pt (135.2 mV dec^{-1}), CNF@Ir (133.5 mV dec^{-1}), CNF@FeNiCo (178.6 mV dec^{-1}), CNF@PtFeNiCo (134.3 mV dec^{-1}), and CNF@PtIrFeNiCo (103.7 mV dec^{-1}). This indicates that introducing the rare-earth metal (REM) element to the CNF@PtIrFeNiCo was able to enhance a kinetic property, which can be explained by the fact that the addition of Ce element into Pt or transition metal (TM) elements increases the anionic electron and lowers the activation energy of electrocatalytic reaction, which accelerate the electrocatalytic performance.[12] REMs, such as Ce, are known to exhibit high oxygen reduction reaction (ORR) properties when forming alloys with Pt and other metals. Due to their unique electronic structure, these alloys, including those with transition metals or precious metals, are also recognized for their improved catalytic activity in HER or OER.[12,13] Through the FTS method, Pt-TM-REM alloys can be easily formed, and it was possible to fabricate metal alloy catalysts with high characteristics.

Electrochemical stability tests were conducted for the CNF@PtFeNiCo, CNF@PtIrFeNiCo, and CNF@PtIrFeNiCoCe; the linear sweep voltammetry (LSV) curves were obtained at 5 mV s^{-1} after the first and 5000th CV cycle at a scan rate of 100 mV s^{-1} (Figure 4c and Figure S14a, Supporting Information). Although the HER LSV curve of the CNF@PtFeNiCo at the first cycle shows low polarization, it was significantly changed along with a large overpotential after the 5000th cycle, which can be attributed to the Pt dissolution during cyclic operation.[14] The CNF@PtIrFeNiCo possesses relatively moderate stability, which may originate from a similar dissolution behavior of Ir metal with Pt. It is found that the CNF@PtIrFeNiCoCe exhibits superior durability even after 5000 cycles, implying that the Ce, which has low reduction potential, provides a stable anodic layer, imparts a less mobile feature of the senary HEA, and prevents the Pt and other elements from dissolution or corrosion into the electrolyte; Ce can be conceived as a less mobile shield against mass transfer through the diffusion and migration with its electrochemical stability.[15]

Besides the HER performance, the OER performance was examined for all the control groups (Figure 4d). It is evident that the CNF@FeNiCo electrocatalyst outperforms other HEA-based electrocatalysts, with an OER onset potential of 1.517 V_{RHE}, an overpotential of 455.6 mV with a current density of 10 mA cm^{-2} at a scan rate of 5 mV s^{-1}. This is particularly noteworthy because the CNF@FeNiCo catalyst does not contain any Ir element that is often considered the most effective catalyst for OER. The homogeneous mixture of Fe, Ni, and Co in the HEA contributes to improving the catalytic activity with low polarization. As expected, the CNF@FeNiCo presents a smaller Tafel slope of 71.5 mV dec^{-1} than other control samples, indicating

© 2023 Wiley-VCH GmbH

15214095, 2023, 46, Downloaded from https://onlinelibrary.wiley.com/doi/10.1002/adma.202305222 by Shanxi University, Wiley Online Library on [06/11/2024]. See the Terms and Conditions (https://onlinelibrary.wiley.com/terms-and-conditions) on Wiley Online Library for rules of use; OA articles are governed by the applicable Creative Commons License

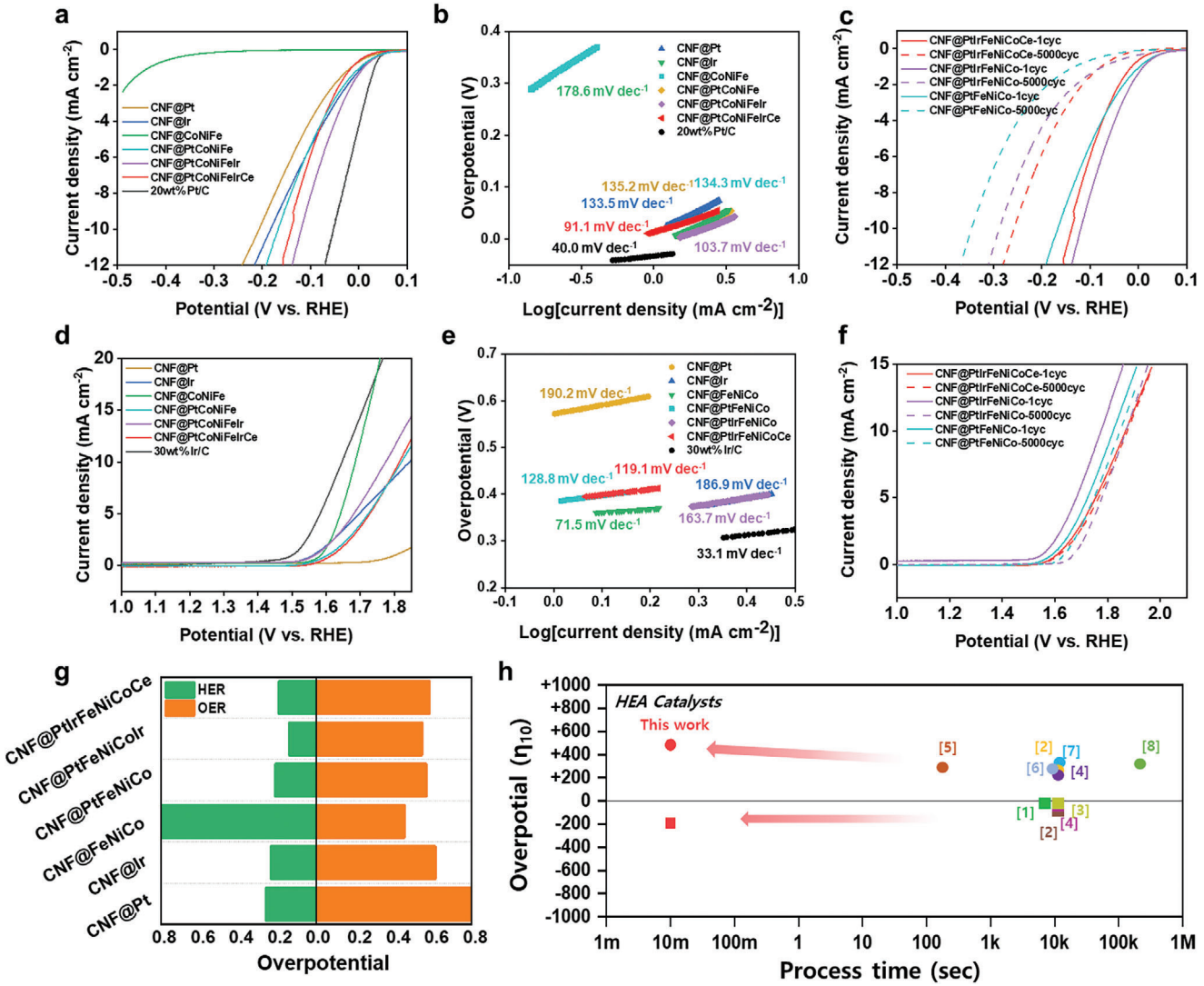

Figure 4. a) HER LSV curves and b) corresponding Tafel plots of HEA catalysts functionalized on CNF with a scan rate of 5 mV s^{-1}. c) The HER LSV curves of CNF@PtFeNiCo, CNF@PtIrFeNiCo, and CNF@PtIrFeNiCoCe with a scan rate of 5 mV s^{-1} after the initial and 5000th CV cycle with a scan rate of 100 mV s^{-1}. d) OER LSV curves and e) corresponding Tafel plots of HEA nanoparticles functionalized on CNFs with a scan rate of 5 mV s^{-1}. f) The OER LSV curves of CNF@PtFeNiCo, CNF@PtIrFeNiCo, and CNF@PtIrFeNiCoCe at 5 mV s^{-1} after the initial and 5000th CV cycle with a scan rate of 100 mV s^{-1}. g) Comparison of the HER and OER overpotentials of CNF@Pt, CNF@Ir, CNF@FeNiCo, CNF@PtIrFeNiCo, and CNF@PtIrFeNiCoCe achieved at 5 mV s^{-1}. h) Comparison of the overpotentials of this work at a scan rate of 5 mV s^{-1} regarding process time to fabricate the catalysts reported previously in the literature.

that the HEA consisting of FeNiCo HEA NPs enabled a dramatic increase in catalyzing OER (Figure 4e). To gain a clear understanding of the mechanisms underlying HEA-based catalysts, we conducted cycling tests of CVs for the CNF@PtFeNiCo, CNF@PtIrFeNiCo, and CNF@PtIrFeNiCoCe catalysts after the first and 5000th CV cycle (as shown in Figure 4f and Figure S14b, Supporting Information). The inclusion of the Ir element in the CNF@PtFeNiCo (purple line) resulted in enhanced OER catalytic activity. However, the Ir atoms might readily dissolve and undergo loss of active sites due to their low electrochemical stability in the electrolyte, which is detrimental to consecutive and repetitive reactions.[16] As for the CNF@PtIrFeNiCoCe, the Ir dissolution was strikingly mitigated by virtue of much more motionless Ce than the others. As a result, the CNF@PtIrFeNiCoCe showed remarkably improved reversibility for 5000 cycles. To explicitly understand the bifunctional electrocatalytic activities for HER and OER, we compared and summarized the overpotentials of the CNF@HEA nanoparticles in Figure 4g. The graph indicates that the relatively inexpensive three components of Fe, Ni, and Co are crucial for achieving bifunctionality for both HER and OER in HEAs, as the HEAs containing these three elements demonstrated high activities for both HER and OER. Besides the bifunctionality, the addition of expensive Pt, Ir, and Ce should be carefully considered and utilized based on their intended purpose, such as to achieve a trade-off between power density and durability for long-term usage. It also has a higher mass activity for noble metal than CNF@Pt. The CNF@PtIrFeNiCoCe also has a higher mass activity for noble metals (Pt and Ir) than CNF@Pt,

 © 2023 Wiley-VCH GmbH

15214095, 2023, 46, Downloaded from https://onlinelibrary.wiley.com/doi/10.1002/adma.202305222 by Shanxi University, Wiley Online Library on [06/11/2024]. See the Terms and Conditions (https://onlinelibrary.wiley.com/terms-and-conditions) on Wiley Online Library for rules of use; OA articles are governed by the applicable Creative Commons License

CNF@Ir, and commercial catalysts (20 wt% Pt/C and 30 wt% Ir/C). In the HER performance, CNF@PtIrFeNiCoCe demonstrated a value of 8.48 A mg^{-1}_{Pt+Ir}, which is ≈12.4 times and 5.8 times higher than that of CNF@Pt (0.68 A mg^{-1}_{Pt}) and commercial Pt/C (1.45 A mg^{-1}_{Pt}), respectively. For OER, it exhibited a mass activity of 7.84 A mg^{-1}_{Pt+Ir}, which is ≈7.3 times and 7.2 times higher than that of CNF@Ir (1.07 A mg^{-1}_{Ir}) and commercial Ir/C (1.09 A mg^{-1}_{Ir}), respectively (Figure S15, Supporting Information). It is confirmed that the synergistic effect of HEA NPs is increased in the OER and HER catalytic performance by replacing noble metal. The comparison data give us explicit direction on how we can rationally design the HEA-based catalyst applied to HER and OER for water splitting. Conclusively, highlighting the extremely short process time within 20 ms to fabricate HEA NPs, we compared the overpotential data of the HEA-functionalized CNFs at a scan rate of 5 m V s^{-1} for HER and OER reported until now (Figure 4h). Our CNF@HEA catalysts with multiple components could be easily synthesized using a fast one-step synthetic approach (Figure S16, Supporting Information), providing effective catalytic sites that are fertile ground for the HER and OER (Table S3, Supporting Information).

3. Conclusion

We have proposed an innovative and synthetic approach for the ultrafast, ambient-air, and large-area processing of HEA NPs through photothermal effects on carbon-based supports, including carbon nanofibers (CNFs), graphene oxides, and MXenes. By exploiting the interaction between light and materials, both conducting and non-conducting substrates with non-connected structures can be utilized, providing considerable freedom for selecting supporting materials. A single 20 ms flash of 4.9 J cm^{-2} on CNFs membrane (diameter of 800 nm) led to momentary high-temperature annealing (>1800 °C and ramping/cooling rates $>10^4$ K s^{-1}), allowing for the successful formation of HEA NPs up to nine elements. In addition, we demonstrated outstanding compatibility for vacuum-free and large-scale synthesis (6.0 × 6.0 cm^2 of CNF paper) with promising potential for mass production. To demonstrate the feasibility of our approach toward applications, we designed and screened senary HEA NPs (PtIrFeNiCoCe) with high activity and excellent stability over 5000 cycles in the water splitting, including hydrogen evolution reactions (HER) and oxygen evolution reactions (OER). We believe that the non-contact interaction between light and support materials can be a breakthrough strategy in realizing a mass- and time-productive approach, demonstrating great potential for high-throughput ambient synthesis of high-entropy catalysts with significantly reduced processing costs. Ultimately, this can contribute to enhancing water splitting and developing high-performance energy-conversion conversion devices.

Supporting Information

Supporting Information is available from the Wiley Online Library or from the author.

Acknowledgements

J.-H.C., S.-H.C., and D.-H.K. contributed equally to this work. This work was supported by the National Research Foundation of Korea (NRF) through Basic Research Program (NRF-2022R1A2B5B02002218912). This work was also supported by grants from the Creative Materials Discovery Program through the National Research Foundation of Korea (NRF) funded by the Ministry of Science and ICT (NRF-2016M3D1A1900035). This work was also supported by the National Research Foundation of Korea (NRF) grant funded by the Korea government (MSIT) (No. RS-2023-00213749). This work was also supproted by Semiconductor-Secondary Battery Interfacing Platform Technology Development Project of NNFC in 2023.

Conflict of Interest

The authors declare no conflict of interest.

Data Availability Statement

The data that support the findings of this study are available from the corresponding author upon reasonable request.

Keywords

ambient air, high-entropy alloys, high-throughput processes, photothermal effects, water splitting

Received: June 1, 2023
Revised: August 4, 2023
Published online: September 22, 2023

[1] a) T. Y. Li, Y. G. Yao, Z. N. Huang, P. F. Xie, Z. Y. Liu, M. H. Yang, J. L. Gao, K. Z. Zeng, A. H. Brozena, G. Pastel, M. L. Jiao, Q. Dong, J. Q. Dai, S. K. Li, H. Zong, M. F. Chi, J. Luo, Y. F. Mo, G. F. Wang, C. Wang, R. Shahbazian-Yassar, L. B. Hu, *Nat. Catal.* **2021**, *4*, 62; b) X. Z. Wang, Q. Dong, H. Y. Qiao, Z. N. Huang, M. T. Saray, G. Zhong, Z. W. Lin, M. J. Cui, A. Brozena, M. Hong, Q. Q. Xia, J. L. Gao, G. Chen, R. Shahbazian-Yassar, D. W. Wang, L. B. Hu, *Adv. Mater.* **2020**, *32*, 2002853.

[2] a) B. Wang, C. Wang, X. Yu, Y. Cao, L. Gao, C. Wu, Y. Yao, Z. Lin, Z. Zou, *Nat Synth* **2022**, *1*, 138; b) P. Xie, Y. Yao, Z. Huang, Z. Liu, J. Zhang, T. Li, G. Wang, R. Shahbazian-Yassar, L. Hu, C. Wang, *Nat. Commun.* **2019**, *10*, 4011; c) T. Y. Li, Y. G. Yao, B. H. Ko, Z. N. Huang, Q. Dong, J. L. Gao, W. Chen, J. G. Li, S. K. Li, X. Z. Wang, R. Shahbazian-Yassar, F. Jiao, L. B. Hu, *Adv. Funct. Mater.* **2021**, *31*, 2010561.

[3] Q. Dong, L. B. Hu, *Chem* **2022**, *8*, 895.

[4] a) Y. G. Yao, Z. N. Huang, P. F. Xie, L. P. Wu, L. Ma, T. Y. Li, Z. Q. Pang, M. L. Jiao, Z. Q. Liang, J. L. Gao, Y. He, D. J. Kline, M. R. Zachariah, C. M. Wang, J. Lu, T. P. Wu, T. Li, C. Wang, R. Shahbazian, L. B. Hu, *Nat. Nanotechnol.* **2019**, *14*, 851; b) Y. G. Yao, F. J. Chen, A. M. Nie, S. D. Lacey, R. J. Jacob, S. M. Xu, Z. N. Huang, K. Fu, J. Q. Dai, L. Salamanca-Riba, M. R. Zachariah, R. Shahbazian-Yassar, L. B. Hu, *ACS Central. Sci.* **2017**, *3*, 294; c) T. Y. Li, Y. G. Yao, Z. N. Huang, P. F. Xie, Z. Y. Liu, M. H. Yang, J. L. Gao, K. Z. Zeng, A. H. Brozena, G. Pastel, M. L. Jiao, Q. Dong, J. Q. Dai, S. K. Li, H. Zong, M. F. Chi, J. Luo, Y. F. Mo, G. F. Wang, C. Wang, R. Shahbazian-Yassar, L. B. Hu, *Nat. Catal.* **2021**, *4*, 439; d) M. J. Cui, C. P. Yang, B. Y. Li, Q. Dong, M. L. Wu, S. Hwang, H. Xie, X. Z. Wang, G. F. Wang, L. B. Hu, *Adv. Energy. Mater.* **2021**, *11*, 2002887.

[5] T. H. Im, J. H. Lee, H. S. Wang, S. H. Sung, Y. B. Kim, Y. Rho, C. P. Grigoropoulos, J. H. Park, K. J. Lee, *Mater. Today* **2021**, *51*, 525.

[6] Y. G. Yao, Z. N. Huang, P. F. Xie, S. D. Lacey, R. J. Jacob, H. Xie, F. J. Chen, A. M. Nie, T. C. Pu, M. Rehwoldt, D. W. Yu, M. R. Zachariah,

 © 2023 Wiley-VCH GmbH

15214095, 2023, 46, Downloaded from https://onlinelibrary.wiley.com/doi/10.1002/adma.202305222 by Shanxi University, Wiley Online Library on [06/11/2024]. See the Terms and Conditions (https://onlinelibrary.wiley.com/terms-and-conditions) on Wiley Online Library for rules of use; OA articles are governed by the applicable Creative Commons License

C. Wang, R. Shahbazian-Yassar, J. Li, L. B. Hu, *Science* **2018**, *359*, 1489.

[7] a) Z. M. Zhang, G. Machin, *Exp. Methods Phys. Sci.* **2009**, *42*, 1; b) R. Sohn, *J. Phys. Conf. Ser.* **2021**, *1826*, 012031.

[8] Y. G. Yao, Z. N. Huang, L. A. Hughes, J. L. Gao, T. Y. Li, D. Morris, S. E. Zeltmann, B. H. Savitzky, C. Ophus, Y. Z. Finfrock, Q. Dong, M. L. Jiao, Y. M. Mao, M. F. Chi, P. Zhang, J. Li, A. M. Minor, R. Shahbazian-Yassar, L. B. Hu, *Matter* **2021**, *4*, 2340.

[9] J. H. Cha, D. H. Kim, C. Park, S. J. Choi, J. S. Jang, S. Y. Yang, I. Kim, S. Y. Choi, *Adv. Sci.* **2020**, *7*, 1903318.

[10] a) H. D. Li, J. P. Lai, Z. J. Li, L. Wang, *Adv. Funct. Mater.* **2021**, *31*, 2106715; b) T. Loffler, A. Ludwig, J. Rossmeisl, W. Schuhmann, *Angew. Chem., Int. Ed.* **2021**, *60*, 26894.

[11] E. Antolini, J. R. C. Salgado, E. R. Gonzalez, *J. Power Sources* **2006**, *160*, 957.

[12] S. Zhang, S. E. Saji, Z. Y. Yin, H. B. Zhang, Y. P. Du, C. H. Yan, *Adv. Mater.* **2021**, *33*, 2005988.

[13] a) C. A. Campos-Roldan, D. J. Jones, J. Roziere, S. Cavaliere, *ChemCatChem* **2022**, 14; b) D. M. F. Santos, C. A. C. Sequeira, D. Maccio, A. Saccone, J. L. Figueiredo, *Int. J. Hydrogen Energy* **2013**, *38*, 3137.

[14] Z. Q. Wang, E. Tada, A. Nishikata, *J. Electrochem. Soc.* **2016**, *163*, C853.

[15] a) D. Santos, L. Amaral, B. Šljukić, D. Macciò, A. Saccone, C. Sequeira, *J. Electrochem. Soc.* **2014**, *161*, F386; b) F. Rosalbino, S. Delsante, G. Borzone, E. Angelini, *J. Electroanal. Chem.* **2008**, *622*, 161.

[16] H. S. Oh, H. N. Nong, T. Reier, A. Bergmann, M. Gliech, J. F. de Araujo, E. Willinger, R. Schlogl, D. Teschner, P. Strasser, *J. Am. Chem. Soc.* **2016**, *138*, 12552.

 © 2023 Wiley-VCH GmbH

15214095, 2023, 46, Downloaded from https://onlinelibrary.wiley.com/doi/10.1002/adma.202305222 by Shanxi University, Wiley Online Library on [06/11/2024]. See the Terms and Conditions (https://onlinelibrary.wiley.com/terms-and-conditions) on Wiley Online Library for rules of use; OA articles are governed by the applicable Creative Commons License